Welding in the World (2024) 68:2293–2309
https://doi.org/10.1007/s40194-024-01754-0

RESEARCH PAPER

Numerical simulation of molten pool behavior and bead formation in Al-alloy GMAW bead-on-plate welding

Yinghao Li[1] · Ran Zong[1] · Yujiao Zhang[1] · Boyang Zhang[1]

Received: 21 June 2023 / Accepted: 8 March 2024 / Published online: 28 March 2024

Abstract
A transient 3D numerical model was established to investigate the multi-coupling transport phenomena in the Al-alloy GMAW bead-on-plate welding process. An integrated self-adaptive distribution mode of "arc current density-arc pressure-electromagnetic force-arc heat" was proposed to adapt to the evolution of the surface morphology of the molten pool. The heat and force state of the molten pool was analyzed to investigate its influence on the bead formation. The results showed that the arc pressure and droplet impingement promoted the backward flow of the liquid metal, thus forming the gouging region. It decreased the concentration of the arc current density, thereby reducing the superheat of the liquid metal and facilitating the filling of the weld toe. Based on the characteristics of the temperature and velocity fields, the characteristics of weld formation in the three stages of arc preheating, melting, and solidification were analyzed. This study revealed the relationship between molten pool behavior and bead formation, promoting the implementation of Al-alloy GMAW in welding and additive manufacturing.

Keywords GMAW · Al-alloy · Numerical simulation · Molten pool behavior · Bead formation

1 Introduction

Aluminum alloys met the requirements for high-quality lightweight components in industries such as aerospace, weapons manufacturing, automotive, and shipping. The gas metal arc welding (GMAW) possessed advantages such as high production efficiency, excellent quality, and low cost, and has been extensively applied in the aluminum alloy manufacturing industry [1]. The welding process involved numerous variables, making it both expensive and challenging to analyze solely through experimental observation data. Numerical simulation of the welding process not only saved costs but also accurately analyzed internal flow fields, temperature fields, and solidification processes in the weld pool, which were difficult to observe through experiments.

Scholars had previously been enthusiastic about simulating the GMAW process of steel. Ohji et al. [2] established a transient three-dimensional model for the GMAW fillet joint, calculating the effects of gravity, surface tension, and arc pressure on the morphology of molten pool. It indicated that the arc pressure was the primary cause of the formation of undercut defects. This model lacked a comprehensive analysis of the role of liquid metal flow in the formation of weld bead. Cho and Farson [3] investigated the physical mechanisms associated with humping phenomenon based on a three-dimensional numerical model. It identified that the formation of thin liquid channel induced by surface tension pinching force, as well as the premature solidification of the melt within the thin channel dividing the weld pool into a front and rear portion, were responsible for humping. Zong et al. [4] characterized the liquid metal behavior during high-speed GMAW by a transient 3D mathematical model. It suggested that the typical processes leading to undercut involve high-velocity backward liquid metal flow, large-size gouging region, and prematurely solidified thin metal layer at weld toe. The aforementioned research provided a comprehensive understanding of the formation mechanism of steel welds. However, aluminum exhibited significant differences from steel in terms of its thermophysical properties, such as high thermal conductivity, low density, and low melting point. This resulted in distinct droplet transfer and molten pool behaviors during GMAW, thereby necessitating independent numerical simulation and analysis for this process.

Recommended for publication by Commission XII - ArcWelding Processes and Production Systems.

✉ Ran Zong
zongran@sdut.edu.cn

[1] School of Mechanical Engineering, Shandong University of Technology, Zibo 255000, People's Republic of China

Currently, some researches had been conducted on the simulation of the aluminum welding process. Bahrnezhad et al. [5] conducted a study on the transient thermal processes and stress fields of aluminum alloy GMAW using a double-ellipsoidal heat source. It analyzed the effects of arc voltage and welding speed on the weld bead structure and mechanical properties. It did not consider the droplet transfer and molten pool flow dynamics, resulting in a certain deviation between the simulated temperature field and the actual results. Ikram et al. [6] established a unified mathematical model of welding arc and pool, and conducted an analysis of the fluid flow and heat transfer. However, the position of the arc remained unchanged, thus making it difficult to quantitatively analyze the impact of the molten pool behavior on the formation of long welds. Murphy et al. [7] proposed a three-dimensional self-consistent model of the arc, workpiece and electrode that included the influence of metal vapor. The enthalpy and momentum transferred by the droplet were found to have a strong influence on the liquid metal flow and weld pool depth. Park et al. [8] performed a numerical simulation of GMAW in the vertical downward position. It pointed that the gravity continuously pushed the liquid metal downward, leading to a swelling of the molten pool at the arc center, which in turn absorbed the momentum transfer, resulting in shallow penetration with a large bead width and low dilution. Murphy and Park conducted their research focusing on the effects of droplet momentum and gravity on the molten pool behavior during the GMAW process, without delving into a comprehensive analysis of arc pressure and surface tension. Zhao et al. [9, 10] established a transient mathematical model to simulate the heat transfer, fluid flow, and geometry morphology in GMAW. It found that the droplet impingement and Marangoni force had the dominated influence on the fluid flow. The liquid metal flowed from center to periphery, and on the bottom of molten pool, a clockwise circulation was formed. Furthermore, Zhao et al. [11] established an integrated three-dimensional model of arc, droplet, and molten pool, pointing out that the increase in the external electromagnetic force led to an increase in the internal flow velocity of the molten pool, an increase in heat dissipation, and a reduction in the size of the molten pool. There had been minimal analysis conducted on the formation mechanism of the weld bead, especially in the context of quasi-steady state.

This study investigated the molten pool behavior in Al-alloy GMAW bead-on-plate welding, using a self-adaptive "arc current density-arc pressure-electromagnetic force-arc heat" integrated model. The distribution of GMAW arc current density, force, and heat on the deformed weld pool surface were quantitatively described. The fluid flow field, temperature filed, and molten pool morphology were investigated, and the reasons for the differences in results compared to steel were explained. The relationships among process parameters, molten pool behavior, and bead formation, including transient and quasi-steady states, were revealed in sequence. The simulation results were verified and agreed well with the experimental results. It provided a guide for further improving Al-alloy GMAW bead-on-plate welding process.

2 Experimental procedure

The Al-alloy GMAW experimental system was composed of a three-axis linkage working platform, a welding power source, a water-cooling system, a wire feeder, and an "image-electrical signal-temperature" synchronous acquisition system, as shown in Fig. 1. The high-speed camera captured the arc shape, droplet transfer, and molten pool at a frame rate of 100 Hz. The current and voltage sensors captured the electrical signals with a frequency of 25 kHz. The thermocouples collected of temperature at the centerline on the back of the weld bead with a frequency of 20 Hz. The welding wire was ER5356 with diameter of 1.2 mm and a composition of Al-4.93 Mg-0.25Si-0.4Fe-0.1Cu-0.1Zn (wt.%). The base metal was 5083 Al-alloy with thickness of 3 mm and a composition of Al-4.8 Mg-0.3Si-0.35Fe-0.1Cu-0.8Mn (wt%). The shielding gas was pure argon. The welding parameters were listed in Table 1.

3 Mathematical model

3.1 Geometric models and thermophysical properties

Figure 2 illustrates the full-scale 3D model of Al-alloy GMAW. In order to reduce the calculation time, only half of the workpiece was taken for modeling, in which the *oxz* plane was the symmetry plane. The model was divided into fluid domain ($0 < y < 7$ mm) and solid domain ($7 < y < 27$ mm). The fluid region was further divided into an upper air phase ($0 < z < 5$ mm) and a lower metal phase ($-3 < z < 0$ mm). The grid was a cube with a side length of 0.2 mm. The welding direction was along the $+x$ axis, and the arc igniting position at (5, 0, 0).

For describing the main characteristics of Al-alloy GMAW and realizing efficient numerical calculation, the simplifications and assumptions were made for the transient 3D model as follows [4]

(1) Due to the symmetry of the workpiece relative to the weld line, only half of the workpiece was taken as the computational domain.

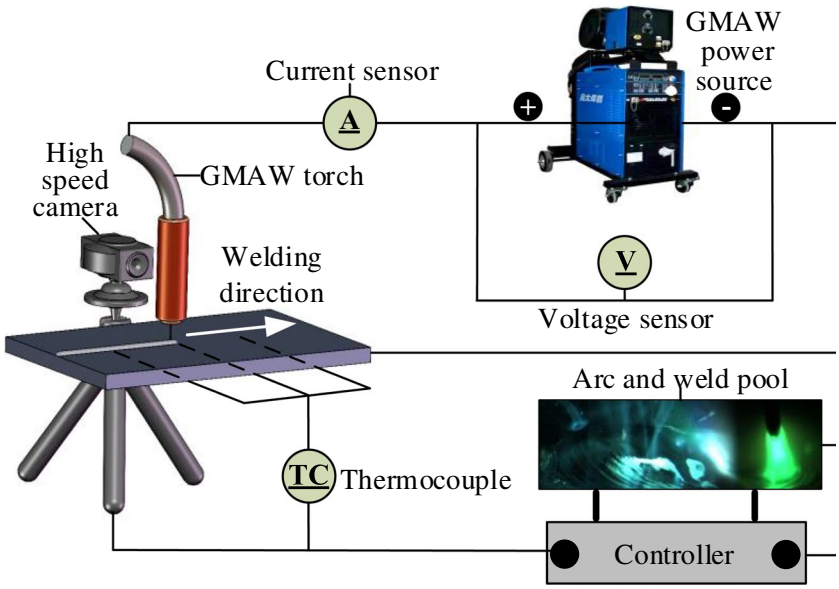

Fig. 1 Schematic diagram of the experimental system

Table 1 Nomenclatures and constants used in the simulation model

Symbol	Nomenclature	Symbol	Nomenclature
a, b	Distribution parameter (mm)	s_t	Surface tension ($N{\cdot}m^{-1}$)
$\mathbf{A}$	Magnetic potential ($N{\cdot}A^{-1}$)	t	Time (s)
$\mathbf{B}$	Magnetic flux density ($N{\cdot}A^{-1}{\cdot}m^{-1}$)	T	Temperature (K)
C	Mushy zone coefficient (1.0×10^{8} m^{-2})	T_S, T_L	Solidus and liquidus temperature (820 K, 902 K)
c_p	Specific heat ($J{\cdot}kg^{-1}{\cdot}K^{-1}$)	T_0	Ambient temperature (300 K)
$\mathbf{f}$	External force source term (N)	T_{drop}	Droplet temperature (975 K)
F	Volume fraction	U	Arc voltage (25 V)
$\mathbf{F_a}^*$	Total arc force (N)	$\mathbf{v}$	Velocity vector ($m{\cdot}s^{-1}$)
f_{L}	Liquid fraction	v_{drop}	Droplet impinging velocity (1.5 $m{\cdot}s^{-1}$)
g	Gravitational acceleration	v_{weld}	Welding speed (0.033 $m{\cdot}s^{-1}$)
h	Enthalpy ($J{\cdot}kg^{-1}$)	v_{wire}	Wire feeding rate (0.18 $m{\cdot}s^{-1}$)
h_c	Heat transfer coefficient (100 $W{\cdot}m^{-2}{\cdot}K^{-1}$)	x, y, z	Coordinates (mm)
I	Welding current (180 A)	β	Volume expansion coefficient (3.66×10^{-5} K^{-1})
$\mathbf{j_a}$	Current density at work piece surface ($A{\cdot}m^{-2}$)	γ	Surface tension ($N{\cdot}m^{-1}$)
$\mathbf{J}$	Current density inside work piece ($A{\cdot}m^{-2}$)	δ	A small number for convergence
K_{dfm}	Controlling parameter for deformed pool surface	ΔL_m	Melting latent heat (3.95×10^{5} $J{\cdot}kg^{-1}$)
K_j, K_p, K_q	Controlling parameter for arc current, force, and heat	ε	Thermal emissivity (0.35)
L_a	Arc length (4.5×10^{-3} m)	η	Thermal efficiency (0.8)
m_s	Mass source term ($kg{\cdot}m^{-3}{\cdot}s^{-1}$)	θ_{e}	Wire tip angle (60 deg)
$\mathbf{n}$	Unit normal vector	λ	Thermal conductivity ($W{\cdot}m^{-1}{\cdot}K^{-1}$)
p	Hydrodynamic pressure (Pa)	μ	Dynamic viscosity ($kg{\cdot}m^{-1}{\cdot}s^{-1}$)
$\mathbf{P_a}$	Arc pressure ($N{\cdot}m^{-2}$)	μ_0	Permeability of vacuum (1.26×10^{-6} $H{\cdot}m^{-1}$)
Q	Arc heat (W)	ρ	Density (2700 $kg{\cdot}m^{-3}$)
$\boldsymbol{q_a}$	Arc heat flux ($W{\cdot}m^{-2}$)	σ	Stefan-Boltzmann constant (5.67×10^{-8} $W{\cdot}m^{-2}{\cdot}K^{-4}$)
r_j, r_q	Distribution radius of arc current and heat (mm)	σ_e	Electrical conductivity ($S{\cdot}m^{-1}$)
r_{wire}	Wire radius (mm)	φ	Electric potential (V)
Q_s	Heat source term ($W{\cdot}m^{-3}$)		

Note: The length unit was in millimeter, and the others were in SI

(2) The molten metal was incompressible, Newtonian, and laminar fluid. The Boussinesq model was used to treat the buoyancy term.
(3) Ignore the volume reduction of liquid metal caused by metal evaporation. Solid-state phase transformations were not considered.
(4) The filler metal and base metal were regarded as the same material, and its thermophysical properties such as thermal conductivity, surface tension, specific heat capacity, viscosity, and conductivity only changed with temperature, as described in Eqs. (1–5). The other physical parameters were constants as listed in Table 1.

$$\lambda[\mathrm{W/(m \bullet K)}] = \begin{cases} 103.47 + 0.1936T - 1.3864 \times 10^{-4} & T \le 820K \\ 185.96.28 - 70T + 0.08871T^2 - 3.75 \times 10^{-5}T^3 & 820K < T \le 820K \\ 57.4935 + 0.003191T & 902K < T \le 975K \\ 53.35 + 0.0035T & T > 975K \end{cases} \tag{1}$$

$$\mathrm{S}_t[\mathrm{N/m}] = \begin{cases} 2 - 3.47 \times 10^{-3}T + 2.42 \times 10^{-6}T^2 & 820K < T \le 902K \\ 1.15368 - 3.367 \times 10^{-4}T & T > 902K \end{cases} \tag{2}$$

$$C_p[\mathrm{J/(kg \bullet K)}] = \begin{cases} 338.98 + 1.539T - 8.027 \times 10^{-4}T^2 & T \le 975K \\ 1076 & T > 975K \end{cases} \tag{3}$$

$$\mu\left[\frac{\mathrm{kg}}{\mathrm{m \bullet s}}\right] = 4.62{\times}10^{-3} - 5.49 \times 10^{-6}T + 1.92 \times 10^{-9}T^2 \qquad T > 820K \tag{4}$$

$$\sigma_e[\mathrm{S/m}] = \begin{cases} 26.45 - 0.03T + 7.9 \times 10^{-6}T^2 & T \le 904K \\ 6.21 - 0.0026T & T > 904K \end{cases} \tag{5}$$

3.2 Governing equations

(1) Mass conservation equation

$$\nabla \bullet \mathrm{v} = \frac{m_s}{\rho} \tag{6}$$

where m_s was the mass source term caused by the droplet transfer which was calculated by Eq. (7).

$$m_s = \pi r_{wire}^2 v_{wire} \rho \tag{7}$$

(2) Momentum conservation equation

$$\rho\left(\frac{\partial \mathrm{v}}{\partial \mathrm{v}} + \mathrm{v}(\nabla \bullet \mathrm{v})\right) = -\nabla p + \mu\nabla^2\mathrm{v} + \mathrm{f} + \mathrm{m}_s\mathrm{v} - \mu C\frac{(1-f_L)^2}{f_L^3 + \delta} \tag{8}$$

where the second-fifth terms on the right side of the equation represented viscous force, external force source term (including electromagnetic force and gravity), droplet momentum, and velocity attenuation in mushy zone. The f_L was the volume fraction of the metal phase in the grid and could be described as follows:

$$f_L = \begin{cases} 0 & T \le T_s \\ \dfrac{T - T_s}{T_L - T_s} & T_s < T < T_L \\ 1 & T \ge T_L \end{cases} \tag{9}$$

(3) Energy conservation equation

$$\rho\left[\frac{\partial h}{\partial t} + \mathrm{v} \bullet \nabla h\right] = \nabla(\lambda\nabla T) + Q_s \tag{10}$$

where the Q_s was the external heat sources (including arc heat, droplet heat, and heat dissipation of molten pool surface through convection and radiation). The h was the mass enthalpy including the fusion latent heat and the sensible heat, which could be expressed as follows:

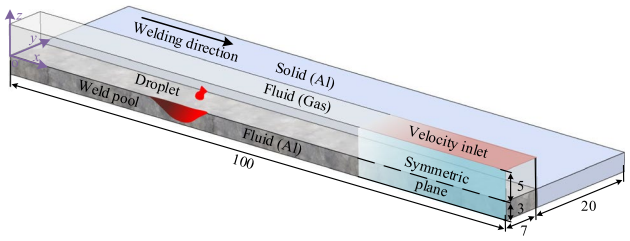

Fig. 2 Full-scale 3D geometry model for GMAW simulation

$$h = \int c_p(T)dT + f_L \Delta L_m \tag{11}$$

(4) Volume fraction (VOF) equation

$$\frac{\partial F}{\partial t} + \nabla \bullet (F\mathrm{v}) = \frac{m_s}{\rho} \tag{12}$$

3.3 Arc thermodynamic model

3.3.1 Current density

The current density distribution on the molten pool surface determined the distribution of arc pressure, electromagnetic force, and arc heat. The metal vapor generated by droplet transfer enhanced the thermal radiation in the arc inner layer, resulting in a decrease in its current density [7, 12]. In addition, the surface of the molten pool directly below the arc center was significantly concave, which increased the distance between the wire tip and the liquid metal. According to the minimum voltage principle, the current density in the arc inner layer would decrease. This made simple Gaussian, double ellipse, and double ellipsoid distribution models unable to accurately describe the distribution of current density in GMAW arc, and a new analytical expression was urgently needed to describe the current density distribution on the 3D weld pool surface.

Zong et al. established an integrated "current density-arc pressure-electromagnetic force-arc heat" self-adaptive distribution model, by assuming the stationary arc to be a "circular cone," in which the arc plasma propagated along a straight line form the wire tip towards the molten pool surface. During high-speed welding, the molten pool moved backwards relative to the arc, and the liquid metal exerted a backward viscous drag force on the arc plasma, causing the "circular cone" to deform and its bottom surface to be no longer a standard circular shape, as shown in Fig. 3a [4]. Initially, on the flat workpiece surface, the current density presented a double ellipse distribution as described in Eq. (13) and shown in Fig. 3b. Then, the weld pool surface changed

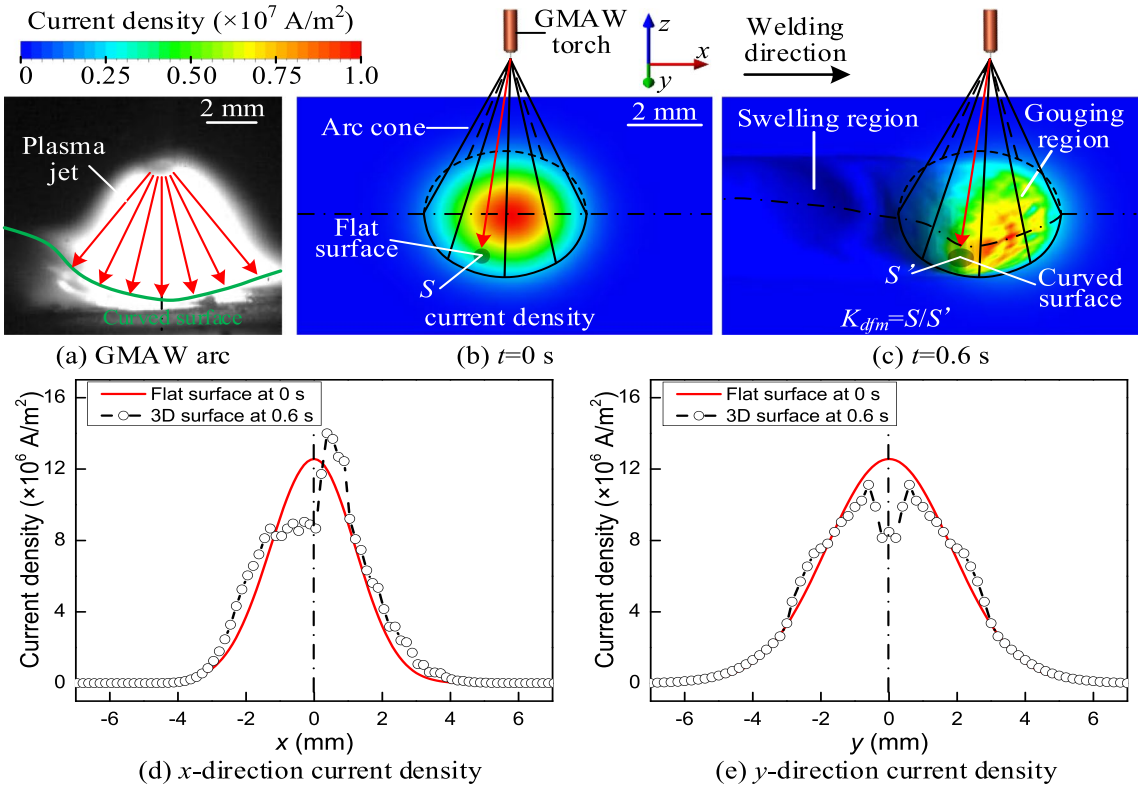

Fig. 3 GMAW arc current density distribution model on molten pool surface

to a curved surface under the action of the arc force and filler metal as shown in Fig. 3c. The spatial distribution of the current lines in the "circular cone" remained unchanged, which meant the number of lines distributed on the area S' was equal to that on the area S. The density of current lines was inversely proportional to the area. This adjustment was realized by the K_{dfm}, as described in Eq. (14). In the gouging region under the arc, the S' was larger than S, and the K_{dfm} was smaller than 1, while in the swelling region, the opposite was true. This was equivalent to reducing the current density at the arc center, as shown in Fig. 3 d and e. The current density distribution showed similar characteristics to those of Murphy and Wang et al.'s arc simulation [7, 12]. Although the model was mathematical convenience, it to some extent demonstrated the influence of metal vapor and minimum voltage principle on the distribution of arc current density. Its accuracy had been verified in the simulation of steel [4].

The K_j in Eq. (13) was a control parameter used to correct the errors caused by discretization and ensure that the integral of current density was equal to the total welding current, as described in Eq. (15). The radius of current density distribution was determined by Eq. (16). The θ_e was the angle of the wire tip, which varied dynamically with the droplet transferred. When the droplet was just formed, the angle might reach up to 100°, and when the droplet detached from the wire tip, it dropped to 20°. The average value of 60° was taken in this model. Considering the backward viscous drag force of the liquid metal on the arc plasma and the restraining effect of the gouging region on the arc, the coefficient a_{jf} and a_{jr} were determined based on the observed front and side images of the arc in the experiment, as described in Eq. (17).

$$\mathrm{j_a}(x,y,z) = K_j \cdot \left[K_{dfm} \cdot \frac{6I}{\pi(a_{jf}+a_{jr})b_j} \cdot \exp\left(-\frac{3(x - v_{weld}t - 0.005)^2}{a_j^2} - \frac{3y^2}{b_j^2} \right) \right] \tag{13}$$

$$K_{dfm}(x,y,z) = S/S' \tag{14}$$

$$\iint_{\Omega} \mathrm{j_a}(x,y,z) \cdot ds - I = 0 \tag{15}$$

$$r_j = \sqrt{(a_{jf}+a_{jr})b_j/2} = 4.36 \times 10^{-4} \times I^{0.289}\theta_e^{0.157} \tag{16}$$

$$a_{jf} = 0.80 \cdot r_j; \quad a_{jr} = 0.85 \cdot r_j; \; a_j = \begin{cases} a_{jf} & x \geq v_{weld}t + 5 \\ a_{jr} & x < v_{weld}t + 5 \end{cases} \tag{17}$$

At the initial moment ($t = 0.0$ s), the current density presented a double elliptic distribution with a radius of 3.7 mm. The peak at the arc center reached 1.0×10^7 A/m^2, as shown in Fig. 3b. At $t = 0.6$ s, the current density was mainly distributed in the gouging region under the arc, where the K_{dfm} was below 1. Considering the integral conservation of current density, the K_j must be bigger than 1. Then, the current density at the bottom of the gouging region decreased, while the current density at the edge increased, as shown in Fig. 3c. The concave surface of the molten pool reduced the concentration ratio of the current density distribution, which would reduce the heat flux and arc pressure in the arc center, and weaken the electromagnetic force in the molten pool.

3.3.2 Arc pressure

The arc pressure was generated by the plasma jet impinging the liquid metal, so the distribution model of arc pressure, such as distribution radius and parameters, was consistent with the current density distribution model, as described in Eq. (18). The K_p was a controlling parameter to ensure the integral of arc pressure was equal to the total arc force $\mathbf{F_a}^*$, as exhibited in Eq. (19). The $\mathbf{F_a}^*$ was proportional to the square of the welding current, as presented in Eq. (20).

$$\mathbf{P_a}(x,y,z) = K_p \cdot (\mu_0 I/4\pi) \cdot \boldsymbol{j_a} \tag{18}$$

$$\iint_{\Omega} \mathbf{P_a}(x,y,za) \cdot ds - \mathbf{F_a^*} = 0 \tag{19}$$

$$\mathbf{F_a^*} = 6.47 \times 10^{-7} I^2 \tag{20}$$

Figure 4 shows the arc pressure distribution. At $t = 0.0$ s, the arc pressure along the x axis was from the arc center to the periphery, and exhibited a bimodal distribution. The front part reached a peak of 50 Pa at $x = 6.5$ mm along the $+x$ axis, and the rear part reached a peak of 200 Pa at $x = 4.0$ mm along the $-x$ axis. The arc pressure along the y axis presented a symmetrical bimodal distribution, pointing from the arc center to the periphery, and reached a peak of 150 Pa at 2 mm from the arc center. The arc pressure along the z axis exhibited a double elliptical distribution, perpendicular to the workpiece surface and vertically downwards, reaching a peak of 800 Pa at the center of the arc.

At $t = 0.6$ s, the deformation of the molten pool surface led to a redistribution of the arc pressure with the change in current density. The front part of the arc pressure along the x axis mainly acted on the surface of the unmelted workpiece and the front wall of the molten pool, where there was very little liquid metal and had a weak impact on the fluid flow inside the molten pool. The rear part acted directly on the liquid metal in the gouging region behind the arc center, promoting the backward flow of the liquid metal. Its peak was located at the bottom of the gouging region, slightly lower than that at $t = 0$ s. The peak of the arc pressure along the y axis was located at the edge of the gouging region, and the pressure around it significantly increased, promoting the lateral spreading of the liquid

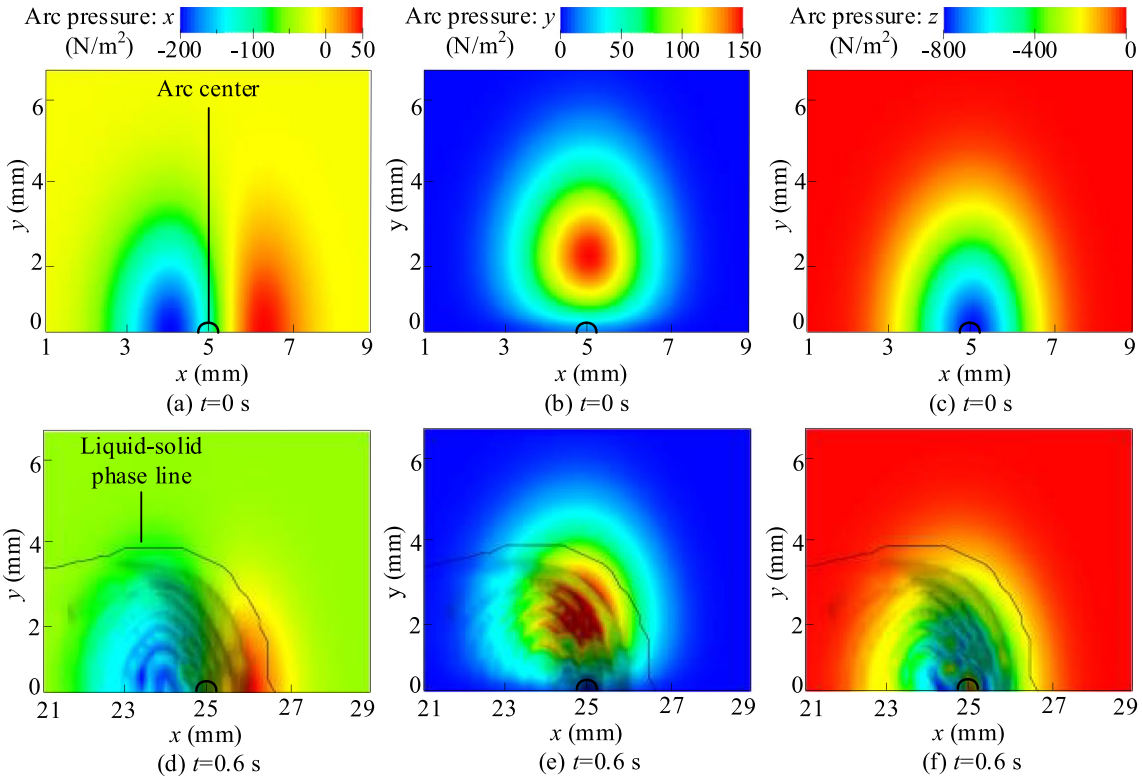

Fig. 4 Arc pressure distribution

metal towards the weld toe. The downward arc pressure along the z axis mainly acted on the gouging region, and compared to that at $t=0.0$ s, its center decreased while the edge increased. Due to the continuity of fluid flow, it still maintained its promoting effect on the backward flow of liquid metal.

The concave surface of the molten pool reduced the concentration ratio of arc pressure, which weakened its promoting effect on the backward flow at the center of the molten pool, and enhanced its promoting effect on the lateral spreading of liquid metal at the weld toe.

3.3.3 Electromagnetic force (EMF)

The electromagnetic force was generated by coupling the electric field inside the molten pool with the magnetic field excited by itself. Four user-defined scalar transport equations were adopted to solve the Maxwell's equations. One was based on Ohm's law to solve the current density distribution inside the work piece, as described in Eq. (21). The arc current that transmitted from the work piece surface to its interior was considered as the source term of Eq. (21), as described by Eq. (22). The other three were used to calculate the magnetic vector potential inside the work piece, as described in Eq. (23). The rotation of the magnetic vector potential was the magnetic flux density, as described in Eq. (24). The current density and the magnetic flux density were known, so electromagnetic force could be calculated based on Fleming's left-hand rule, as described in Eq. (25).

$$\boldsymbol{J} = -\sigma_e \nabla \varphi \tag{21}$$

$$-\nabla \cdot (\sigma_e \nabla \varphi) = \nabla \cdot \boldsymbol{j_a} \tag{22}$$

$$-\nabla^2 A_x = \mu_0 J_x;\ -\nabla^2 A_y = \mu_0 J_y;\ -\nabla^2 A_z = \mu_0 J_z \tag{23}$$

$$\boldsymbol{B} = \nabla \times \boldsymbol{A} \tag{24}$$

$$F_{\mathrm{magx}} = J_y B_z - J_z B_y,\ F_{\mathrm{magy}} = J_z B_x - J_x B_z,\ F_{\mathrm{magz}} = J_x B_y - J_y B_x \tag{25}$$

Figure 5 illustrates the electromagnetic force distribution. At $t=0.0$ s, the electromagnetic force along the x axis was from the arc periphery to the center, and exhibited a bimodal distribution. The front part reached a peak of 2000 N/m^3 at $x=6.5$ mm. The rear part reached a peak of 2000 N/m^3 at $x=4.0$ mm. The electromagnetic force along the y axis presented a symmetrical bimodal distribution, pointing from the arc center to the periphery, and reached a peak of 2000 N/m^3 at 2 mm from the arc center. The electromagnetic force along the z axis exhibited a circular distribution, perpendicular to the workpiece surface and vertically downwards, reaching a peak of 2000 N/m^3 at 2 mm from the arc center.

At $t=0.6$ s, the deformation of the molten pool surface led to a redistribution of the electromagnetic force. The front

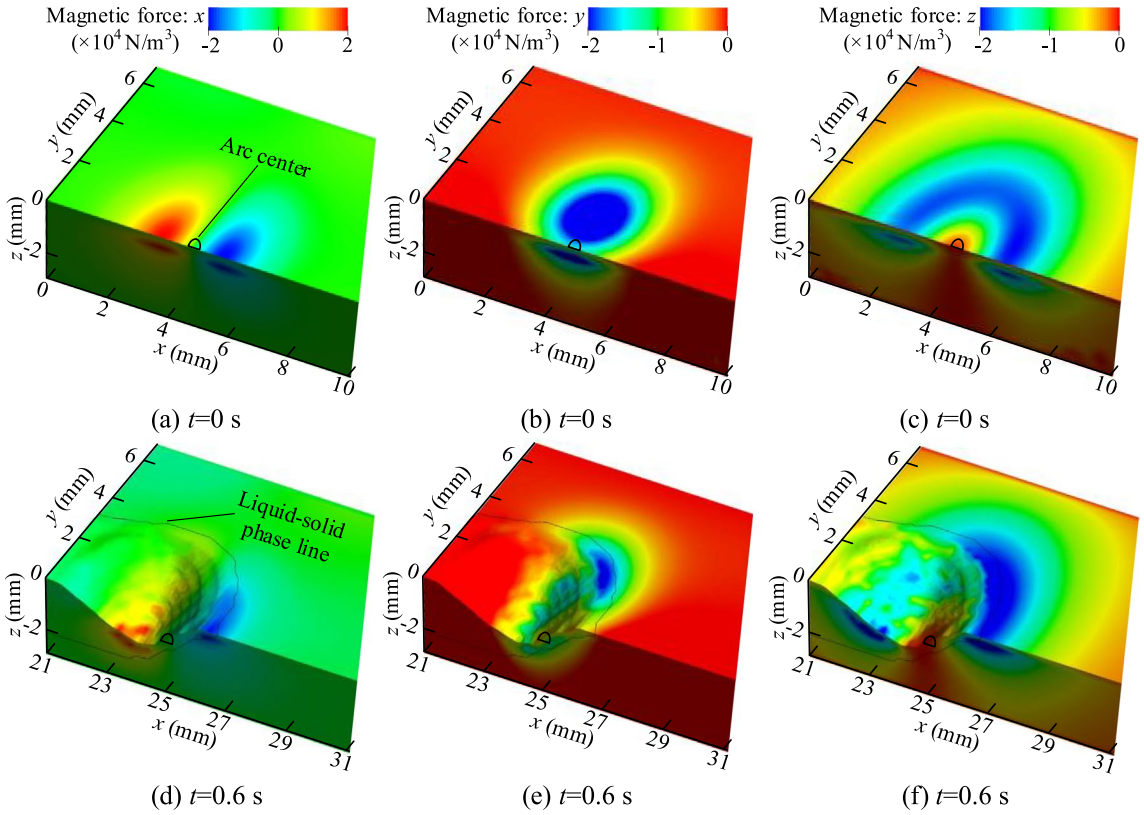

Fig. 5 Electromagnetic force distribution

part of the electromagnetic force along the x axis mainly acted on the surface of the unmelted workpiece and the front wall of the molten pool, and had little impact on the liquid metal flow. The rear part acted directly at the bottom of gouging region, suppressing the backward flow of the liquid metal. The peak of the electromagnetic force along the y axis was located at the edge of the gouging region, and suppressed the lateral spreading of the liquid metal. There was a strong electromagnetic force downward along the z axis in both the gouging region and the weld toe. Due to the continuity of fluid flow, it promoted the backward flow of liquid metal.

The concave surface of the molten pool significantly reduced the electromagnetic force in the gouging region, weakening its suppressing effect on the backward flow of liquid metal. There was no significant change in the electromagnetic force at the welding toe, which promoted the inward contraction of the liquid metal.

3.3.4 Arc heat

The arc heat distribution mainly depended on the current density of the molten pool surface. Its patterns, including the distribution coefficients a_{qf} and a_{qr}, were the same as current density, as described in Eqs. (26) and (27). However, it was also influenced by the thermal radiation from the arc space. Based on the study of Tsai, the arc heat distribution radius was slightly larger than that of the current density, as described in Eq. (28) [13]. The controlling parameter K_q was used to ensure that the integral of heat flux was equal to the total arc heat Q, namely, welding heat input minus droplet enthalpy, as described in Eqs. (29) and (30).

$$q_a(x,y,z) = K_q \cdot \left[K_{dfm} \cdot \frac{6Q}{\pi\left(a_{qf}+a_{qr}\right)b_q} \cdot exp\left(-\frac{3\left(x - v_{\text{weld}}t - 0.005\right)^2}{a_q^2} - \frac{3y^2}{b_q^2} \right) \right] \tag{26}$$

$$a_{qf} = 0.80 \cdot r_q;\ a_{qr} = 0.85 \cdot r_q;\ a_q = \begin{cases} a_{qf}\ x \geq v_{\text{weld}}t + 0.005 \\ a_{qr}\ x < v_{\text{weld}}t + 0.005 \end{cases} \tag{27}$$

$$r_q = \sqrt{\left(a_{qf}+a_{qr}\right)b_q/2} = 9.23 \times 10^{-3} \times I^{0.2645} L_a^{0.3214} \tag{28}$$

$$\iint_{\Omega} \mathrm{q_a}(\mathrm{x},\mathrm{y},\mathrm{z}) \cdot ds - Q = 0 \tag{29}$$

$$Q = \eta UI - \rho h\left(\pi v_{\text{wire}} r_{\text{wire}}^2\right) \tag{30}$$

Figure 6 shows the heat flux distribution. At t=0.0 s, the heat flux presented a double elliptic distribution with a radius of

5.6 mm. The peak at the arc center reached 7.5×10^7 W/m^2. At t=0.6 s, both the gouging region and weld toe were covered by the heat flux. The K_{dfm} was less than or equal to 1. Considering the integral conservation, the K_q must be bigger than 1. Then, the heat flux at the bottom of the gouging region decreased, while at the weld toe increased. The concave surface of the molten pool reduced the concentration ratio of the heat flux, which would reduce the superheat of the liquid metal under the arc center and slow down the cooling rate of the liquid metal at the weld toe.

3.4 Boundary conditions

The boundary conditions for temperature, velocity, electric potential, and magnetic vector potential in the numerical model were shown in Table 2. The model was divided into a solid domain and a fluid domain. The boundaries of the fluid domain included the upper, bottom, front, rear face, and fluid–solid interface.

The upper surface was set as a velocity inlet for the droplet, as shown in Fig. 7. At the wire tip, the temperature was 1300 K, and the velocity changed periodically at the frequency of f_{drop}. During one droplet transfer cycle (t_1–t_7), it could be divided into two stages based on speed, with a speed of 1.5 m/s during t_1–t_4 and a speed of zero during t_4–t_7. The duration of t_1–t_4 was equal to $v_{wire}/(v_{drop}{\cdot}f_{drop})$. At the rest area except for the wire tip, the temperature was 300 K and the speed remained zero.

For the electric and magnetic fields, air is considered to be an electrical insulator since its electrical conductivity is zero. Therefore, the boundaries for electric and magnetic vector potential on the upper surface were both "flux = 0."

The bottom, front, rear surface, and fluid–solid interface were solid walls in the fluid domain, whose velocity was

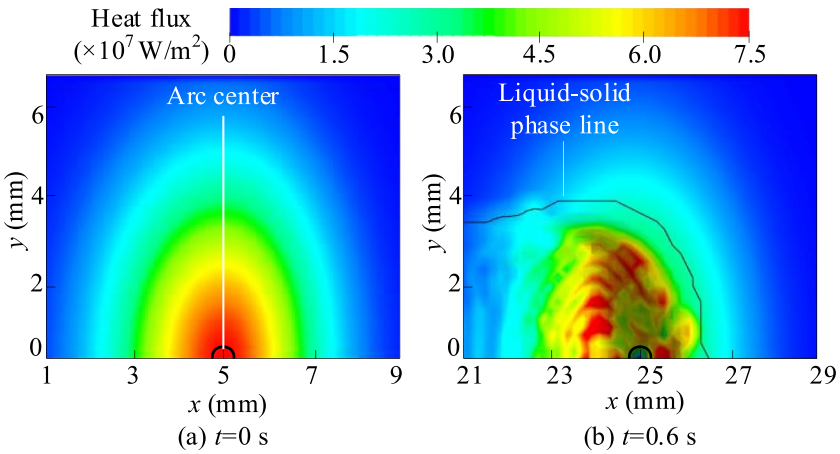

Fig. 6 Arc heat flux distribution

Table 2 Numerical model boundary conditions

		Temperature	Velocity	Electric potential	Magnetic vector potential
Upper surface	Wire tip	$T = T_{drop}$	$v = v_{drop}/v = 0$	$\partial\varphi/\partial\boldsymbol{n} = 0$	$\partial\boldsymbol{A}/\partial\boldsymbol{n} = 0$
	Rest area	T = 300 K	v = 0		
Bottom surface		$-\lambda(\partial T/\partial\boldsymbol{n}) = -h_c\nabla T - \varepsilon\sigma(T^4 - T_0^4)$	v = 0	$\partial\varphi/\partial\boldsymbol{n} = 0$	$\partial\boldsymbol{A}/\partial\boldsymbol{n} = 0$
Front/rear surfaces		$-\lambda(\partial T/\partial\boldsymbol{n}) = -h_c\nabla T - \varepsilon\sigma(T^4 - T_0^4)$	v = 0	$\varphi = 0$	$\boldsymbol{A} = 0$
Fluid–solid interface		Coupled	v = 0	$\varphi = 0$	$\boldsymbol{A} = 0$
Solid surface		$-\lambda(\partial T/\partial\boldsymbol{n}) = -h_c\nabla T - \varepsilon\sigma(T^4 - T_0^4)$	None	None	None

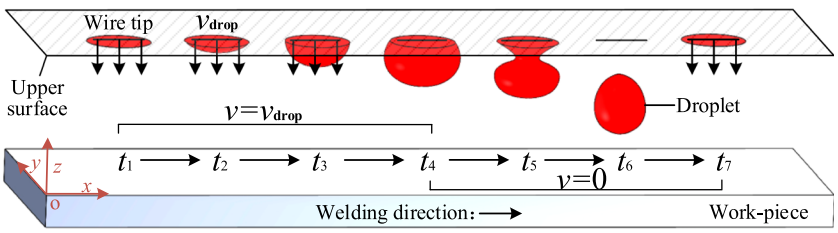

Fig. 7 Schematic sketch of droplet transfer

zero. The interface temperature was solved based on heat conduction, did not require additional boundary condition. The bottom, front, and rear surfaces were based on convection and radiation. In actual welding, the four corners of the workpiece were fastened on the workbench, and there was a groove directly below the weld bead. As the width and length of the workpiece were much larger than the thickness, it was considered that the bottom surface was insulated. The boundaries for electric and magnetic vector potential at the bottom surface were both "flux = 0," and the boundaries at the front, rear surface, and fluid–solid interface were "value = 0."

In the solid domain, only the temperature field were considered as the rapid decay of electromagnetic fields in space. The temperature boundary of the solid surface was the same as the other solid walls in the fluid domain.

4 Simulation results and analysis

4.1 Verification of the model

Figure 8 shows the evolution of average temperature and volume of molten pool over time. The calculation of temperature only considered grids filled with liquid metal, as described by Eq. (31). The volume was the integral of the liquid metal, as described by Eq. (32).

$$T_{\text{avg}} = \iiint_{\Omega} (f_L \cdot F_1 \cdot T) dV / V_{\text{pool}} \tag{31}$$

$$V_{\text{pool}} = \iiint_{\Omega} (f_L \cdot F_1) dV \tag{32}$$

Initially, high-temperature droplets converged on the surface of the workpiece to form a small molten pool, with a temperature of up to 960 K. High-temperature droplets and arc heat melted the base metal, resulting in a rapid increase in the volume and a rapid decrease in temperature, reaching a quasi-steady state at 0.5 s. The simulated results with a grid size of 0.2 mm were compared with the results of 0.25 mm and 0.30 mm. The evolution process of temperature and volume was highly consistent, with an error of less than 2%. It proved that the model with a grid size of 0.20 mm was sufficient to ensure the accuracy of the calculation.

Figure 9 illustrates the comparison between experimental and simulated results on the molten pool morphology, bead cross-section, and thermal cycle. The molten pool was teardrop shaped, with a gouging region under the arc and a swelling at the tail, as shown in Fig. 9a. The length of the molten pool was approximately 10 mm, and the width was slightly greater than 8 mm. The angle between the fusion line direction and the horizontal plane in the cross-section

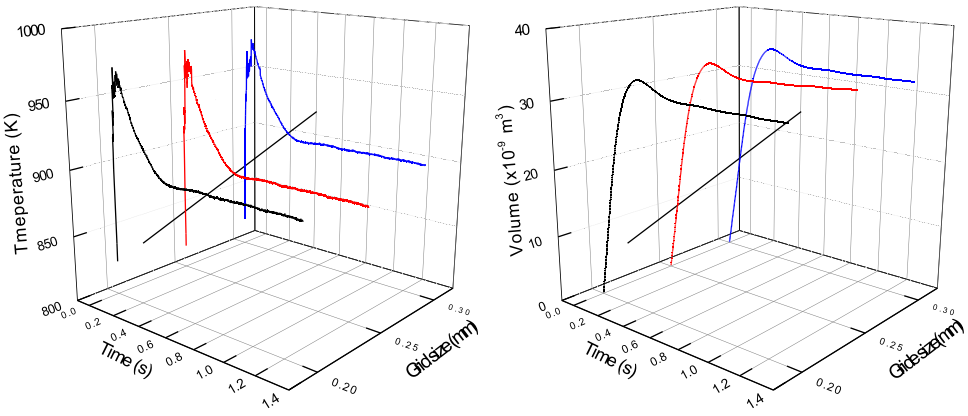

Fig. 8 Variation of average temperature and volume of molten pool over time

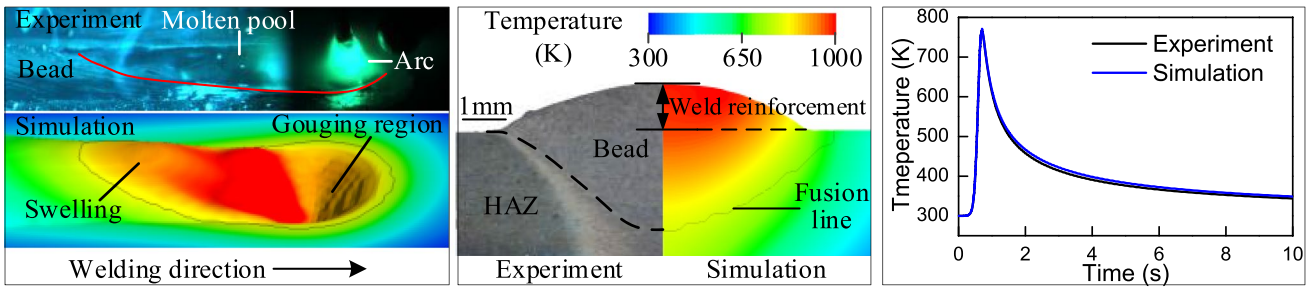

(a) Molten pool (b) Weld bead cross section (c) Thermal cycles

Fig. 9 Comparison of experimental and simulated results

Table 3 Comparison of experimental and simulation results

	Experiment	Simulation	Relative error (%)
Molten pool length (mm)	9.97	10.20	2.25
Width (mm)	8.39	8.20	1.07
Penetration (mm)	2.33	2.30	1.28
Weld reinforcement (mm)	1.15	1.13	1.74
Max. temperature (K)	765	775	1.31

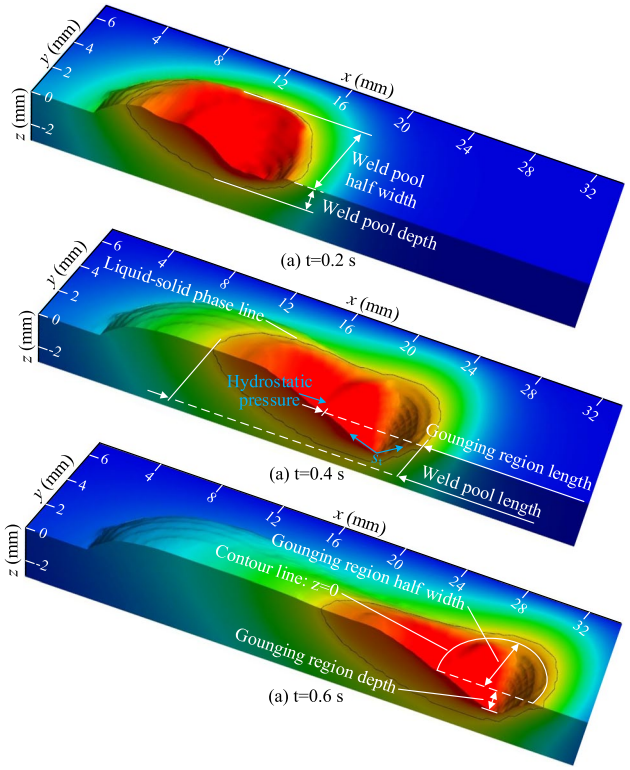

Fig. 10 Temperature fields on the upper surface and in the longitudinal section of the molten pool

was approximately 30°, as shown in Fig. 9b. The penetration of the molten pool was approximately 2.3 mm, and the reinforcement was about than 1.1 mm. The maximum temperature of the thermal cycle at the centerline on the back of the weld bead was about 770 K, as shown in Fig. 9(c). The detailed data was listed in Table 3. The relative errors were controlled within 3%. It proved the rationality of the numerical model.

4.2 Morphology and temperature field of molten pool

Figure 10 illustrates the morphology and temperature field of molten pool on the upper surface and longitudinal section. According to its evolution characteristics, its growth process could be divided into three stages: the rapid expanding stage (stage I, $t < 0.2$ s), the slow expanding stage (stage II, $0.2 < t < 0.5$ s), and the quasi-steady stage (stage III, $t > 0.5$ s), as shown in Fig. 11.

In the stage I, the volume of the molten pool was smaller and the liquid metal was mainly composed of high temperature filler metal. At 0.2 s, the high-temperature area was large and the average temperature was above 920 K, as described in Fig. 10a. The size of the molten pool and the gouging region increased sharply under the action of the superheated droplet and arc heat, as shown in Fig. 11. Both the molten pool length and width increased at a rate of 4.3×10^{-2} m·s^{-1}, and the penetration increased at a rate of 8.0×10^{-3} m·s^{-1}, reaching 8.6 mm, 8.6 mm, and 1.6 mm, respectively, at 0.2 s. The increase rate of molten pool volume was 2.8×10^{-7} m^3·s^{-1}, which was larger than the melting rate of welding wire (2.0×10^{-7} m^3·s^{-1}). The increase rate of the length, width, and depth of the gouging region was 1.9×10^{-2} m·s^{-1}, 2.6×10^{-2} m·s^{-1}, and 4.5×10^{-3} m·s^{-1}, reaching 3.8 mm, 5.2 mm, and 0.9 mm at 0.2 s, respectively. The main reason was that the surface deformation of the molten pool under the arc was relatively small, and the gouging region was shallow. The K_{dfm} was slightly less than 1, and the arc heat and force concentration were high, which would drive the liquid metal to flow backward at a high speed and melt the base metal rapidly. The variation trends of aluminum alloy molten pool and steel of GMAW in the first stage were

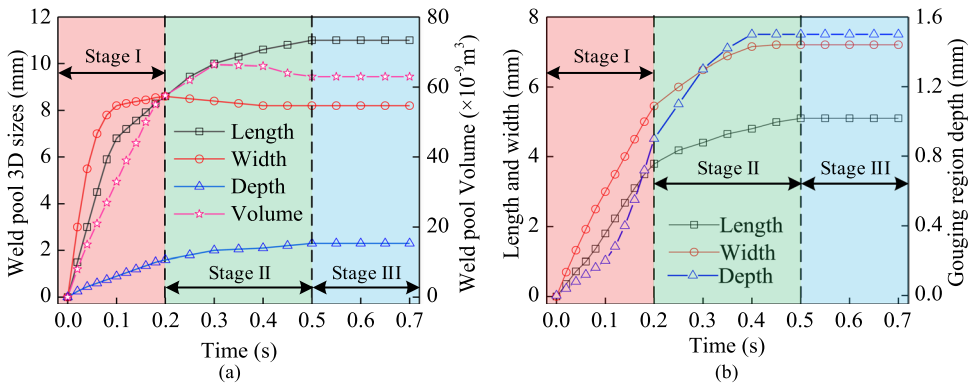

Fig. 11 Sizes of **a** molten pool and **b** gouging region

similarly. Due to the fact that the temperature of aluminum alloy molten pool was much lower than that steel, and the physical properties of the aluminum alloy varied less with temperature, the welding process was easier to approach quasi-steady state. The time spent in the stage I was only half that of steel [4].

In the stage II, the average temperature of liquid metal decreased from 920 to 890 K, as described in Fig. 10b. The sizes of molten pool and gouging region slowly increased, as shown in Fig. 11. The increase rates of the length and depth of molten pool reduced to 8.0×10^{-3} m·s^{-1} and 2.3×10^{-3} m·s^{-1}, respectively. The width of molten pool did not change significantly. The molten pool volume increased from 5.7×10^{-8} m^3 to 6.6×10^{-8} m^3, and the increasing rate was only 3.0×10^{-8} m^3·s^{-1}, which was far less than the melting rate of the welding wire. Compared with steel, aluminum alloy had high thermal conductivity, fast heat dissipation in the molten pool, and the molten metal was more prone to solidification. It indicated that the solidification rate of the liquid metal reached a balance with the melting rate of the base metal and the welding wire [4]. The growth rate of length, width, and depth of the gouging region decreased to 4.3×10^{-3} m·s^{-1}, 6.7×10^{-3} m·s^{-1}, and 2.0×10^{-3} m·s^{-1}, and reached 5.0 mm, 7.2 mm, and 1.5 mm at 0.5 s, respectively. This could be explained by the significant concave-convex deformation of the molten pool surface. On the one hand, the liquid metal surface of the gouging region was concave, and the surface tension generated an upward force to suppress the increase in surface area, as shown in Fig. 10b. On the other hand, the accumulation of liquid metal behind the arc formed a convex surface, and the hydrostatic pressure forced the liquid metal to backfill the gouging region. The K_{dfm} in the concave zone was less than 1. The arc heat and force concentration decreased. Its effect on the backward flow and base metal melting was weakened.

In the stage III, the liquid metal solidified at the rear of the molten pool, and the base metal and welding wire continuously melted under the arc. The solidification rate and melting rate were the same, and the morphology and sizes of the molten pool remained unchanged. The gouging region achieved a dynamic equilibrium under the joint action of arc force, electromagnetic force, surface tension, and hydrostatic pressure.

It found that the sizes of the molten pool and gouging region showed a high degree of consistency in variation. The rate of increase in length, width, and depth gradually decreased over time. The width and depth reached quasi-steady state at 0.4 s, while the length continued to increase under the action of inertial force and reached quasi-steady state at 0.5 s. The high-temperature molten pool always lagged behind the arc. This was because these liquid metal was heated by the arc and accumulated the heat from the droplets. It solidified rapidly in the rear of the molten pool, which carried a high risk of causing cracks [14].

4.3 Velocity field of molten pool

The arc pressure, droplet impingement, inertia force, surface tension, Marangoni force, electromagnetic force, and hydrostatic pressure determined the liquid metal flow, which had a significant effect on the weld bead formation [4]. Figure 12 illustrates the flow patterns on the upper surface and longitudinal section of the molten pool. Specifically, it could be divided into backward flow (No. 1) and lateral spreading (No. 2) in the front of the molten pool, and forward reflux (No. 3) at the tail of the molten pool. Figure 13 shows the changes in average velocity, flow intensity and velocity ratio over time. The average velocity was decomposed into three components: backward flow, lateral spreading, and forward reflux mentioned above. The flow intensity was the absolute sum of the three components of average velocity. The velocity ratio was divided into lateral to backward and forward to backward.

In the stage I, the arc pressure and droplet impingement acted on the shallow gouging region, overcoming surface tension, and pushing the liquid metal to spread laterally, as shown in Fig. 12 a and b. The liquid metal layer below the arc was relatively thick, and the downward momentum of the molten droplets was mainly converted into the lateral direction momentum [8]. The heat of the droplet was transferred to the bottom of the base metal with downward momentum, and the depth of the molten pool gradually increased. At 0.2 s, the volume of the molten pool was small, the depth of the molten pool reached 1.44 mm. The velocity of the liquid metal was affected by the droplet impingement, resulting in significant fluctuations, as shown in Fig. 13(a). The liquid metal flowed backwards along the streamline "1" with a velocity of 0.126 m/s. Due to the continuity of fluid flow, the average velocity of lateral spreading reached 0.133 m/s along the streamline "2." The width of molten pool rapidly increased. At the weld toe, the surface tension hindered the lateral spreading. The length of molten pool rapidly increased, and the liquid metal accumulated at the rear of the molten pool to form a swelling. The surface tension and hydrostatic pressure obstructed backward flow and transformed it into a forward flow inside the molten pool along the streamline "3," as shown in the red dotted box. The reflux velocity was 0.100 m/s. But due to the strong digging effect of the arc pressure, the gouging region could not be filled, and its size rapidly increased.

In the stage II, the gouging region had been formed, as shown in Fig. 12 c and d. The welding process gradually reached a quasi-steady state, and the depth of the molten pool increased to 2.13 mm, the buffering effect of the liquid metal thin layer below the arc on the droplet momentum was

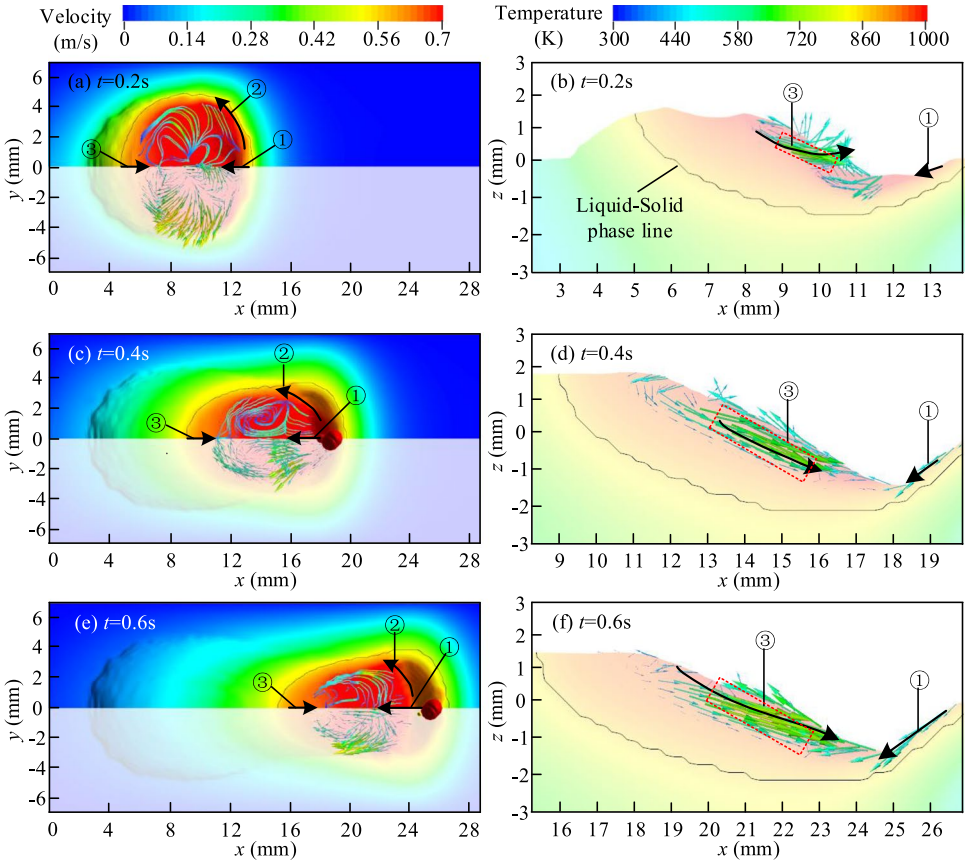

Fig. 12 Velocity field on the upper surface and longitudinal section of the molten pool

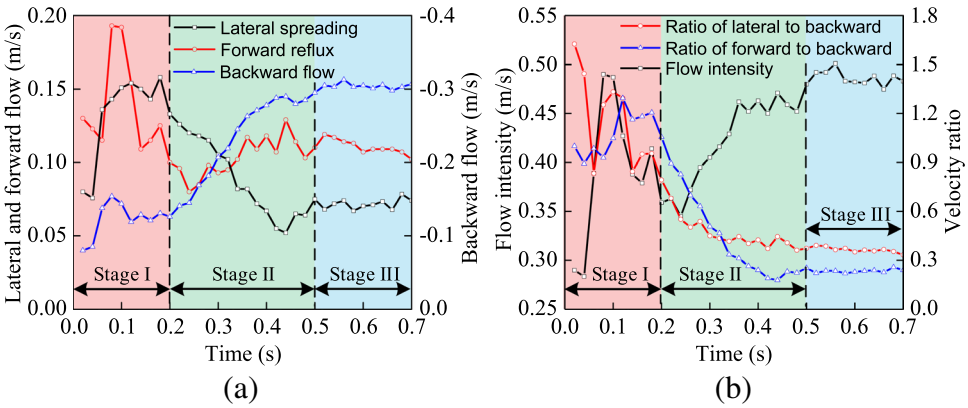

Fig. 13 **a** Average velocity, and **b** flow intensity and velocity ratio

weakened, and the droplet impact momentum was mainly converted into backward flow [8]. The average velocity of lateral spreading and forward reflux continued to decrease, while the backward flow velocity increased rapidly. The flow intensity was enhanced, and backward flow dominated. At 0.4 s, the droplet impinged the inclined front wall of the molten pool at 1.5 m/s. Its downward momentum was converted into backward momentum, as described by streamline "1." It was hindered by the liquid metal reflux along the weld centerline, and could only flow along the side wall channels ($y < -2$ mm and $y > 2$ mm), as shown in streamline "2." The lateral spreading velocity decreased to 0.067 m/s, and the molten pool width no longer increased. The backward flow velocity increased to 0.278 m/s, but was later hindered by the swelling at the rear of the molten pool. It turned to flow forward along the weld centerline, as shown in streamline "3." The molten pool length slowly increased. The reflux velocity increased to 0.118 m/s, partially offsetting the arc digging effect, so the sizes of the gouging region slowly increased.

In the stage III, the droplet impingement caused weak periodic fluctuations under the arc, but it could not change the macroflow patterns of the molten pool, as

shown in Fig. 12 e and f. The lateral spreading velocity was about to 0.071 m/s. The liquid metal flowed backward at an average velocity of 0.304 m/s along the side wall channels to the rear of the molten pool driven by arc pressure and droplet impingement. Then, under the action of surface tension and hydrostatic pressure caused by the swelling, liquid metal turned to flow forward at an average velocity of 0.111 m/s along the weld centerline. The backward flow velocity was decreased by 40% compared to steel, and the velocity aspect ratio was significantly reduced, as shown in Fig. 13(b), which was conducive to lateral spreading and filling of the weld toe [15]. The weld bead had no undercut defects, as shown in Fig. 9.

The flow field in the molten pool was significantly affected by droplet impingement in the stage I, with significant fluctuations and chaotic flow. The influence of droplet impact momentum on the velocity inside the molten pool was related to the thickness of the liquid metal layer below the arc. In the stage I, the liquid metal layer under the arc was thick, and the momentum generated by the droplet impingement was mainly converted into lateral momentum, while a small portion was converted into forward and backward momentum of the liquid metal. The downward momentum of the molten metal enhanced the transfer of heat from the droplets to the bottom of the workpiece, which gradually increased the depth of the molten pool. The welding process gradually reached stability, and the depth of the molten pool increased by 48% compared to the stage I. Then, the liquid metal layer under the arc became thinner, reducing the buffering effect on droplet impact. The momentum of droplet impact was mainly converted into backward flow velocity. High-temperature filler metal accumulated at the tail of the molten pool, which was an important cause of hump and undercut defects during high-speed welding. As the volume of the molten pool increased, the fluctuation weakened and each streamline remained stable, ensuring the stability of weld bead formation.

4.4 Weld bead formation

When the simulation process reached 0.5 s, the aforementioned molten pool's temperature, volume, sizes, and flow field indicated that the welding process had reached a quasi-steady state, with the arc center positioned at $x = 21.7$ mm. The weld cross-section $x = 26.7$ mm had not yet entered the significant thermal influence range of the arc and droplet. Its melting and solidification process could represent the weld bead formation at quasi-steady state, which was helpful for understanding the formation mechanism of long weld bead, as shown in Fig. 14. Figure 15 shows the weld bead temperature, backward flow velocity, liquid–solid phase line, and fusion line dimensions at different times. The temperature was taken as the average value of the grid in the weld bead. The backward flow velocity was taken as the average value of the grid in the melting zone. Based on their characteristics, the process was divided into three stages: arc preheating (stage IV, $0.5 < t < 0.6$ s), melting (stage V, $0.6 < t < 0.7$ s), and solidification (stage VI, $0.7 < t < 1.0$ s).

In the stage IV, the arc center moved from $x = 21.7$ mm to $x = 25.0$ mm, and the cross-section $x = 26.7$ mm was heated by the arc. At 0.6 s, the weld bead temperature reached 821 K, forming a thin liquid metal at the surface, as shown in Fig. 14a. The arc pressure pointed towards the $+x$ axis. But under the action of surface tension, the liquid metal flowed backward at a velocity of 0.012 m/s, as shown in Fig. 15a. The phase line coincided with the fusion line, and the sizes rapidly increased, as shown in Fig. 15b. Under the preheating effect of the arc, there was no obvious depression on the surface of the workpiece.

In the stage V, the arc center moved from $x = 25.0$ mm to $x = 28.3$ mm, just sweeping the cross-section $x = 26.7$ mm. During 0.60–0.65 s, the cross-section was subjected to arc heat, resulting gouging region. The depth of the molten pool reached 1.3 mm, and the temperature of the molten pool slowly increased to 910 K. At 0.65 s, the 98th droplet, counting from the initial droplet, immerged into the molten pool just at this cross-section, bringing a large amount of heat and momentum, as shown in Fig. 14b. The temperature rapidly increased. The heat of the droplet was transferred to the bottom of the base metal at the downward speed, and the volume of the thin layer of metal below the arc decreased; the penetration increased. Arc pressure and droplet impingement overcame surface tension and gravity, driving the liquid metal to flow backward at 0.158 m/s, as shown in Fig. 15a. The sizes of phase line and fusion line rapidly increased, as shown in Fig. 15b. Then, another seven droplets immerged into the molten pool at the front of this cross-section. At 0.7 s, the average temperature of the weld bead reached a peak of 983 K. The momentum of droplet impact was converted into backward flow velocity in the molten pool; the backward flow velocity reached a peak of 0.307 m/s, which meant that the amount of metal flowing out was greater than the amount flowing in. The penetration reached 2.1 mm, indicating that the increase in molten pool depth was related to the thermal effect of the droplets on the molten pool. Under the action of arc and droplet, the surface of the workpiece rapidly melted and depressed to form a molten pool, as shown in Fig. 14c.

In the stage VI, the arc center moved from $x = 28.3$ mm to $x = 38.3$ mm. The cross-section $x = 26.7$ mm lagged behind the direct action of the arc and droplet. The effect

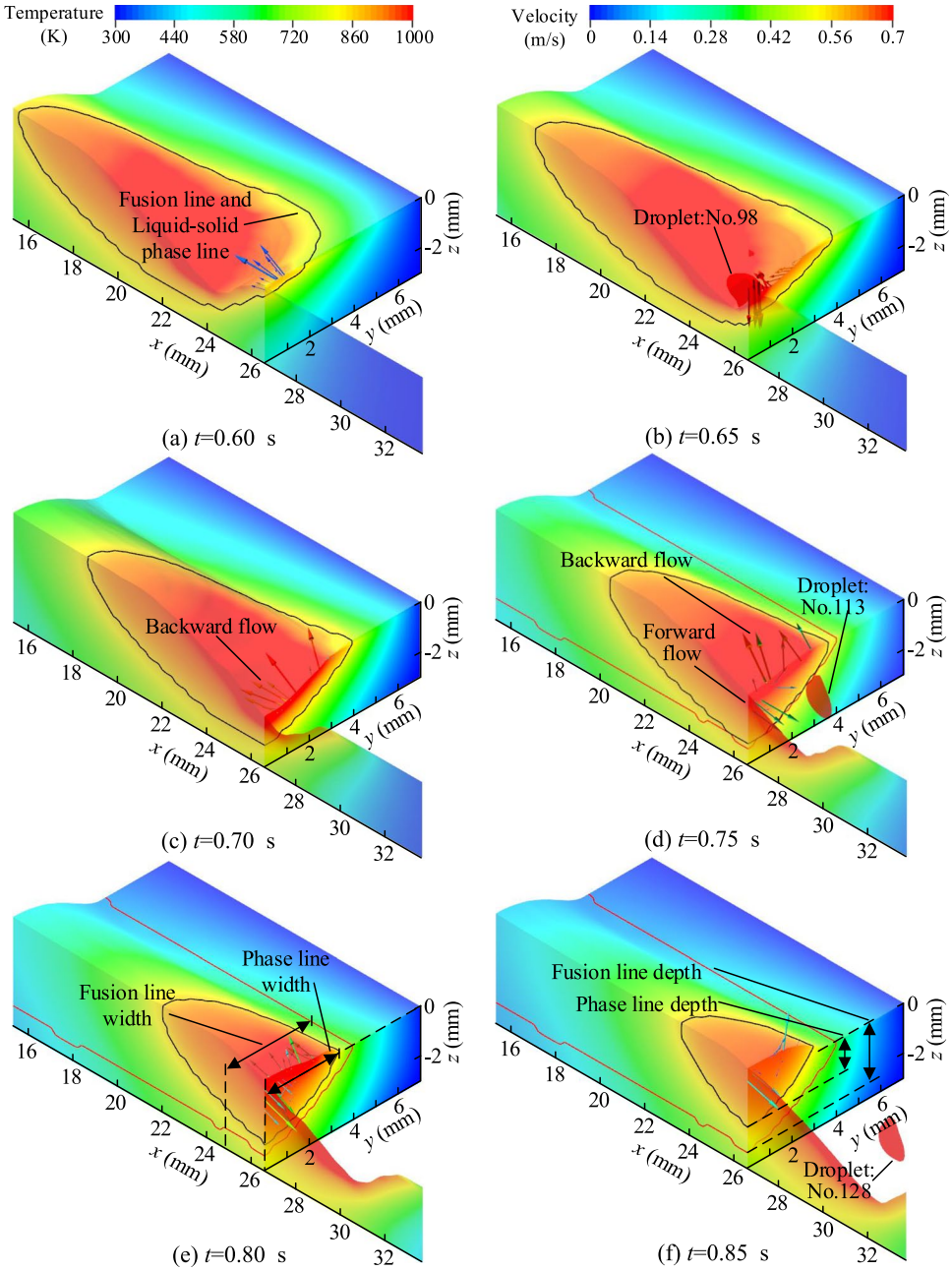

Fig. 14 Weld bead formation process at cross-section $x = 26.7$ mm

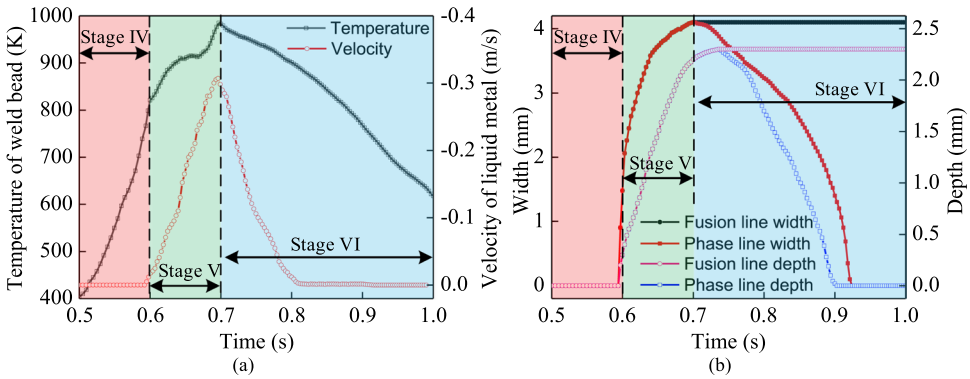

Fig. 15 **a** Temperature and backward flow velocity, and **b** sizes of the fusion line and phase line

of 105th droplet on the heat and force of the section was significantly reduced. The temperature and velocity continued to decrease. The liquid metal solidified at the liquid–solid phase line, reducing its width and depth. At 0.75 s, the swelling at the tail of the molten pool hindered backward flow, and generated a forward reflux under the action of inertial force and hydrostatic pressure, as shown in Fig. 14d. The backward flow velocity dropped to 0.113 m/s, which meant that the amount of metal flowing in was greater than the amount flowing out. The depression was filled and formed a protrusion, as shown in Fig. 14 e and f. At 0.85 s, the weld bead temperature decreased to 840 K. The fluidity of liquid metal was weak, and the morphology of the weld bead no longer changed.

The process for forming aluminum alloy weld bead was similar to that for steel. The cross-section underwent drastic changes in temperature and velocity from initial melting to complete solidification, in which the surface tension, arc pressure, droplet impingement, inertial force, and hydrostatic pressure played a crucial role [4]. Aluminum alloys had a higher thermal conductivity and lower melting point than steel, so the cooling of the liquid metal was faster. The melting to solidification process of the cross section lasted about 0.3 s, only half of the steel. When aluminum alloy transformed from liquid to solid, its ability to dissolve gases sharply decreased. The high cooling rate resulted in insufficient time for the gas to spill out from the liquid metal, leading to an increase in the likelihood of pore formation [16]. This meant that during the aluminum alloy welding process, the surface of the workpiece should be cleaned more strictly than steel, and external air should be well isolated.

5 Conclusions

(1) Arc heat, arc force, and electromagnetic force were usually calculated separately in traditional Gaussian distribution models, and it was difficult to adjust to account for the deformation of molten pool surface. The dual elliptical integrated arc heat and arc force distribution model used in this article unifies the distribution of arc heat, arc force, and electromagnetic force. There was no longer limited by the shape of the molten pool surface. It can more accurately describe the thermal distribution of the GMAW molten pool surface with large surface deformation. The accuracy of the numerical model was verified through experiments.

(2) The liquid metal flowing back along the side wall channels at an average velocity of 0.3 m/s, which is only half of the backward flow velocity of steel under the same welding current. It allowed sufficient time for the high-temperature filler metal to spread towards the weld side, and the temperature gradient at the weld toe is significantly lower than steel. There was sufficient liquid metal and sufficient time to fill the weld toe, which avoided undercut defects.

(3) The process of weld forming was analyzed from the perspectives of temperature field and flow field through a quasi-steady state cross-section, which had important reference value for the mechanism of weld formation in long welds. The impact of heat accumulation on the numerical model during the long welding process will be conducted in the following work.

Funding This work was supported by the Shandong Provincial Natural Science Foundation (grant number ZR2023ME139), National Natural Science Foundation of China (grant numbers 51905321), and Shandong Provincial Key Laboratory of Precision Manufacturing and Non-traditional Machining.

Data availability Data available on request from the authors.

Declarations

Disclaimer We also declare that we do not have any commercial or associative interest that represents a conflict of interest in connection with the work entitled "Numerical simulation of molten pool behavior and bead formation in Al-alloy GMAW bead-on-plate welding."

Conflict of interest The authors declare no competing interests.

References

1. Wang XW, Huang Y, Zhang YM (2013) Droplet transfer model for laser-enhanced GMAW. Int J Adv Manuf Technol 64:207–217. https://doi.org/10.1007/s00170-012-4014-6
2. Ohji T, Tsuji Y, Miyasaka F, Yamamoto T (2001) Mathematical modeling of metal active gas (MAG) arc welding. J Mater Sci Technol (Shenyang, China) 17:167–168. http://kns.cnki.net/KCMS/detail/detail.aspx?dbcode=CJFD&filename=CLKJ200101084
3. Cho MH, Farson DF (2007) Understanding bead hump formation in gas metal arc welding using a numerical simulation. Metall Mater Trans B 38:305–319. https://doi.org/10.1007/s11663-007-9034-5
4. Zong R, Chen J, Wu C (2021) Numerical analysis of molten metal behavior and undercut formation in high-speed GMAW. J Mater Process Tech 297:117266. https://doi.org/10.1016/j.jmatprotec.2021.117266
5. Baharnezhad S, Golhin AP (2017) In-situ measurement and finite element simulation of thermo-mechanical properties of AA6063 aluminum alloy for MIG weldment. Mater Phys Mech 32:222–236. https://doi.org/10.18720/MPM.3222017_15
6. Ikram A, Chung H (2021) Numerical simulation of arc, metal transfer and its impingement on weld pool in variable polarity gas metal arc welding. J Manuf Process 64:1529–1543. https://doi.org/10.1016/j.jmapro.2021.03.001
7. Murphy AB, Thomas DG (2017) Prediction of arc, weld pool and weld properties with a desktop computer model of metal-inert-gas welding. Weld World 61(3):623–633. https://doi.org/10.1007/s40194-017-0444-y

8. Park JH, Cho DW, Moon HS (2022) CFD simulation of molten pool dynamic behavior on vertical-downward position in P-GMAW process. Int Commun Heat Mass 132:105876. https://doi.org/10.1016/j.icheatmasstransfer.2021.105876
9. Zhao W, Cao X, Du X, Wei Y, Liu R, Chen J (2022) Numerical simulation of heat and mass transfer in CMT-based additive manufacturing. J Mech Eng 58:267–276. https://kns.cnki.net/kcms/detail/11.2187.TH.20211116.1647.006.html
10. Zhao WY, Wei YH, Long JW, Chen JC, Liu RP, Ou WM (2021) Modeling and simulation of heat transfer, fluid flow and geometry morphology in GMAW-based wire arc additive manufacturing. Weld World 65:1571–1590. https://doi.org/10.1007/s40194-021-01123-1
11. Zhao WY, Jin HX, Du XW, Chen JC, Wei YH (2022) A 3D arc-droplet-molten pool integrated model of Al alloy GMAW process: heat transfer, fluid flow and the effect of external magnetic field. Vacuum 202:111129. https://doi.org/10.1016/j.vacuum.2022.111129
12. Wang LL, Wang HP, Lu FG, Murphy AB, Carlson BE (2014) Numerical analysis of Al vapour effects in gas metal arc welding of Al alloys. Sci Technol Weld Join 19(5):361–368. https://doi.org/10.1179/1362171814Y.0000000200
13. Tsai NS, Eagar TW (1985) Distribution of the heat and current fluxes in gas tungsten arcs. Metall Trans B 16:841–846. https://doi.org/10.1007/BF02667521
14. Kou S (2015) A criterion for cracking during solidification. Acta Mater 88:366–374. https://doi.org/10.1016/j.actamat.2015.01.034
15. Zong R, Chen J, Wu C, Padhy GK (2017) Influence of molten metal flow on undercutting formation in GMAW. Sci Technol Weld Joining 22:198–207. https://doi.org/10.1080/13621718.2016.1214406
16. Mathers G (2002) The welding of aluminium and its alloys. Woodhead Publishing, Cambridge, England